Chapter 9
Nonlinear Deformations of Soft Tissues for Surgery Simulation

Yongmin Zhong, Bijan Shirinzadeh, Julian Smith, Chengfan Gu, and Aleksandar Subic

Abstract Soft tissue deformation is of great importance to virtual reality based surgery simulation. This paper presents a new methodology for modelling of nonlinear soft tissue deformation from the physicochemical viewpoint of soft tissues. This methodology converts soft tissue deformation into nonlinear chemical–mechanical interaction. Based on this, chemical diffusion of mechanical load and non-rigid mechanics of motion are combined to govern the dynamics of soft tissue deformation. The mechanical load applied to a soft tissue to cause a deformation is incorporated in chemical diffusion and distributed among mass points of the soft tissue. A chemical diffusion model is developed to describe the distribution of the mechanical load in the tissue. Methods are established for construction of the diffusion model on a 3D tissue surface and derivation of internal forces from the distribution of the mechanical load. Real-time interactive deformation of virtual human organs with force feedback has been achieved by the proposed methodology for surgery simulation. The proposed methodology not only accommodates isotropic, anisotropic and inhomogeneous materials by simply modifying diffusion coefficients, but it also accepts local and large-range deformation.

Keywords Soft tissue deformation • Virtual reality • Surgery simulation • Chemical diffusion and force feedback

Y. Zhong (✉) • C. Gu
School of Aerospace, Mechanical and Manufacturing Engineering, RMIT University, Melbourne, VIC, Australia
e-mail: yongmin.zhong@rmit.edu.au

B. Shirinzadeh
Department of Mechanical and Aerospace Engineering, Monash University, Melbourne, VIC, Australia

J. Smith
Department of Surgery, Monash Medical Centre, Monash University, Melbourne, VIC, Australia

A. Subic
Swinburne Research & Development, Swinburne University of Technology, Hawthorn, VIC, Australia
e-mail: aleksandar.subic@rmit.edu.au

R.N. Jazar, L. Dai (eds.), *Nonlinear Approaches in Engineering Applications*,
DOI 10.1007/978-3-319-27055-5_9

9.1 Introduction

Simulation of soft tissues is a challenging research topic in surgery simulation. Surgery simulation requires soft tissues react to the applied forces in a realistic fashion and in real time. However, due to the complex nonlinear behaviours of soft tissues, it is difficult to handle both of these conflicting requirements (Costa 2012; Zhu and Gu 2012; Zhong et al. 2012). Currently, most of the existing deformation methods are fully built on an elastic model. The common methods such as mass-spring (San-Vicente et al. 2012; Patete et al. 2013; Omar et al. in press), FEM (Finite Element Method) (Taylor et al. 2011; Zhang et al. 2014; Mafi and Sirouspour 2014) and BEM (Boundary Element Method) (Zhu and Gu 2012; Duarte et al. 2011) are mainly built on linear elasticity. Linear elastic models are simple and allow reduced runtime computations. However, they only allow displacements to be less than 10 % of the soft object size (Fung 1993), and thus cannot handle the nonlinear behaviours of soft tissues. Although nonlinear elastic models can handle nonlinear material properties, it is very difficult to satisfy the real-time requirement of soft tissue deformation due to the complexity and extremely expensive computational nature of nonlinear elastic models. So far, research on large-range nonlinear deformations of soft tissues is insufficient owing to the complex soft tissue behaviour and insufficient tissue response information (Taylor et al. 2011).

This paper presents a new methodology for modelling of nonlinear soft tissue deformation by using chemical–mechanical interaction. This methodology combines nonlinear chemical diffusion of mechanical load with non-rigid mechanics of motion to govern the simulation dynamics of soft tissue deformation. The mechanical load applied to a soft tissue to cause a deformation is incorporated in chemical diffusion as a chemical load, and is further distributed among mass points of the soft tissue. A chemical diffusion model is developed to describe the distribution of the mechanical load in the soft tissue. Numerical methods are presented for construction of the chemical diffusion model on a 3D tissue surface. A gradient method is established for deriving internal forces from the distribution of the mechanical load. Interactive deformation of anatomical models of human body with force feedback has been achieved for surgery simulation. Examples are presented to demonstrate the efficacy of the proposed methodology.

9.2 Related Work

A considerable amount of research efforts have been directed towards the area of soft tissue simulation. The most popular method is the mass-spring model (San-Vicente et al. 2012; Patete et al. 2013; Omar et al.), in which a deformable object is discretized into a system of mass points connected by springs. The advantage of the mass-spring model is that the computation is less time consuming

and the algorithm is easier to implement. However, the mass-spring model does not allow accurate modelling of material properties, and increasing the number of springs leads to a stiffer system.

FEM (Taylor et al. 2011; Zhang et al. 2014; Mafi and Sirouspour 2014) and BEM (Zhu and Gu 2012; Duarte et al. 2011) are the typical methods focused on accurate modelling of soft tissue deformation. In FEM or BEM, rigorous mathematical analysis based on continuum mechanics is applied to accurately model the mechanical behaviours, namely the stress–strain relationship of a soft tissue by decomposing it into a number of volume elements or boundary elements. However, these methods are computationally expensive and only the simplest variants such as linear shape functions have been used in soft tissue simulation. Although the computational performance can be improved by the explicit FEM (Zhang et al. 2014; Mafi and Sirouspour 2014) and pre-computation technique (Peterlik et al. 2010), the use of linear elasticity cannot accommodate nonlinear large-range deformation.

Studies were reported to handle large-range nonlinear deformation. These methods are not built on real nonlinear elasticity, and they are mainly focused on incorporation of nonlinear elements into linear elastic models to achieve large-range deformation. Picinbono et al. reported an explicit nonlinear FEM to handle large-range deformation by using nonlinear strains (Picinbono et al. 2003). However, the use of quadric strains generally requires very expensive computations for real-time simulation, and the runtime assembly of all the force terms for every element limits the interactivity to only a few hundred elements. Although the expensive computations caused by the use of the nonlinear strains can be handled by utilizing a subspace integration method (Barbic and James 2005), the use of nonlinear strains can only model geometric nonlinearity rather than nonlinear material properties. Schwartz et al. reported a FEM model by introducing two nonlinear Lame material constants for soft tissue simulation (Schwartz et al. 2005). However, the improvement does not comply with the constitutive laws of materials, since the Lame material constants are the inherent properties of materials and they are not changeable constants. The stiffness warping method was also reported to handle nonlinear large-range deformation (Etzmuss et al. 2003; Choi and Ko 2005; Cakir and Yazici 2009). However, the warping method can only handle geometric nonlinearity due to the use of the geometric improvement based on linear elasticity. Liu et al. reported a method by incorporating nonlinear internal forces into the linear mass-spring model to deal with nonlinear properties of soft tissues (Patete et al. 2013). Although it can handle large-range deformation, this method is still limited to the linear strain–stress relationship. Zhu and Gu also reported a hybrid deformable model, in which the traditional BEM was combined with the mass-spring model to deal with large-range deformation (Zhu and Gu 2012). However, due to the use of BEM, this method still replies on the pre-computation technique to achieve the real-time performance.

Recently, the authors studied soft tissue deformation by using a physical process, such as autowaves (Zhong et al. 2006a), cellular neural network (Zhong et al. 2006b), heat conduction (Zhong et al. 2010) and reaction–diffusion process

(Wu and Herzog 2002). These methods mainly rely on the analogies between elastic deformation and the nonlinear physical processes. Although experiments are conducted to verify the analogies, additional computational theoretical work is required to further support the analogies.

9.3 Chemical Diffusion of Mechanical Load

Behaviours of soft tissues are not only mechanically governed, but they also depend on physicochemical events (Lai et al. 1991). In fact, soft tissues form a system consisting of different particles such as mobile ions, and the soft tissue behaviours are associated with the ion concentration in the interstitium (Myers et al. 1984). When a rise in ion concentration is imposed on a tissue previously at equilibrium, ions diffuse into the tissue and move through the tissue matrix. The gradients of the concentrations are the driving forces for ion movement, and the movement of ions controls most of the compressive properties of soft tissues (Myers et al. 1984; Chou and Pagano 1967). Therefore, from the physicochemical viewpoint, soft tissue behaviours are an effect induced by ion diffusion activities.

According to the continuum theory, conservation of ions requires

$$\frac{\partial \rho}{\partial t} + \nabla \cdot (\rho \mathbf{v}) = 0 \tag{9.1}$$

where ρ is the ion density at time t, $\nabla\cdot$ is the divergence operator and $\mathbf{v}$ is the average velocity of ion diffusion.

Since

$$\rho = MC \tag{9.2}$$

where C is the ion concentration and M is the ion mass.

Equation (9.1) becomes

$$\frac{\partial C}{\partial t} + \nabla \cdot (C\mathbf{v}) = 0 \tag{9.3}$$

The ion diffusion may be described by Fick's law

$$-\omega \nabla C = C\mathbf{v} \tag{9.4}$$

where ω is the diffusion coefficient and ∇ is the gradient operator.

Combining Eq. (9.4) with Eq. (9.1) results in the governing equation of the chemical diffusion process

$$\frac{\partial C}{\partial t} = \nabla \cdot (\omega \nabla C) \tag{9.5}$$

If ions are generated by a chemical load, Eq. (9.5) becomes

$$\frac{\partial C}{\partial t} + H = \nabla \cdot (\omega \nabla C) \tag{9.6}$$

where H represents the ion density under a chemical load.

When a soft tissue is deformed under a mechanical force, work is done by the mechanical force. The deformation is the consequence of applying the load generated by the mechanical force to the soft tissue. The load is absorbed in the soft tissue in the form of strain energy to deform the soft tissue away from its natural state (Chou and Pagano 1967; Sadd 2005). According to the first law of thermodynamics, the mechanical load applied to the soft tissue can be treated as an equivalent chemical load to inject ions into the tissue. Therefore, the ion density H can be defined as the strain energy density

$$H = \int \boldsymbol{\sigma} \, d\varepsilon \tag{9.7}$$

where $\boldsymbol{\sigma}$ is the stress and $\boldsymbol{\varepsilon}$ is the strain at the contact point.

Since the mechanical load is only applied at the contact point, the resultant ion density is set only at the contact point where the mechanical load is applied, while the values of the ion density at other points are set to zero. In addition, it is not difficult to see from Eqs. (9.6) and (9.7) that soft tissue deformation is described as chemical diffusion of the mechanical load, which is applied to a soft tissue to cause a deformation.

To solve Eq. (9.6), it is necessary to determine the boundary conditions. The boundary conditions determine the character of the ion interchange over the boundary. Here, we choose the Neumann boundary condition as shown in Eq. (9.8), which implies that there is no energy loss at the boundary.

$$\frac{\partial C}{\partial \mathbf{N}_\Gamma} = 0 \tag{9.8}$$

where $\mathbf{N}_\Gamma$ is an outward normal vector at the boundary Γ.

9.4 Model Establishment

The chemical diffusion model can be constructed on a 3D surface or a 3D volume. For the sake of simplicity and without loss of generality, we consider the construction of the chemical diffusion model on a 3D surface.

The construction of the chemical diffusion model on a regular grid such as a rectangular grid is straightforward. The discrete chemical diffusion model on a rectangular grid can be easily established by using a finite difference scheme. For an internal point $\mathbf{P}_{i,j}$ in a rectangular grid, the discrete chemical diffusion model at point $\mathbf{P}_{i,j}$ may be written as

$$\begin{aligned} C_{i,j}(t+\Delta t)=C_{i,j}(t)&+\frac{2\omega C_{i+1,j}(t)\Delta t}{\left\|\overrightarrow{\mathbf{P}_{i,j}\mathbf{P}_{i+1,j}}\right\|\left(\left\|\overrightarrow{\mathbf{P}_{i-1,j}\mathbf{P}_{i,j}}\right\|+\left\|\overrightarrow{\mathbf{P}_{i,j}\mathbf{P}_{i+1,j}}\right\|\right)}+\frac{2\omega C_{i-1,j}(t)\Delta t}{\left\|\overrightarrow{\mathbf{P}_{i-1,j}\mathbf{P}_{i,j}}\right\|\left(\left\|\overrightarrow{\mathbf{P}_{i-1,j}\mathbf{P}_{i,j}}\right\|+\left\|\overrightarrow{\mathbf{P}_{i,j}\mathbf{P}_{i+1,j}}\right\|\right)}\\ &+\frac{2\omega C_{i,j+1}(t)\Delta t}{\left\|\overrightarrow{\mathbf{P}_{i,j}\mathbf{P}_{i,j+1}}\right\|\left(\left\|\overrightarrow{\mathbf{P}_{i,j-1}\mathbf{P}_{i,j}}\right\|+\left\|\overrightarrow{\mathbf{P}_{i,j}\mathbf{P}_{i,j+1}}\right\|\right)}+\frac{2\omega C_{i,j-1}(t)\Delta t}{\left\|\overrightarrow{\mathbf{P}_{i,j-1}\mathbf{P}_{i,j}}\right\|\left(\left\|\overrightarrow{\mathbf{P}_{i,j-1}\mathbf{P}_{i,j}}\right\|+\left\|\overrightarrow{\mathbf{P}_{i,j}\mathbf{P}_{i,j+1}}\right\|\right)}\\ &-\frac{2\omega C_{i,j}(t)\Delta t}{\left\|\overrightarrow{\mathbf{P}_{i-1,j}\mathbf{P}_{i,j}}\right\|\left\|\overrightarrow{\mathbf{P}_{i,j}\mathbf{P}_{i+1,j}}\right\|}-\frac{2\omega C_{i,j}(t)\Delta t}{\left\|\overrightarrow{\mathbf{P}_{i,j-1}\mathbf{P}_{i,j}}\right\|\left\|\overrightarrow{\mathbf{P}_{i,j}\mathbf{P}_{i,j+1}}\right\|}-H_{i,j}\Delta t \end{aligned} \tag{9.9}$$

where $\left\|\overrightarrow{\mathbf{P}_{i-1,j}\mathbf{P}_{i,j}}\right\|$ and other similar terms represent the magnitudes of vector $\overrightarrow{\mathbf{P}_{i-1,j}\mathbf{P}_{i,j}}$ and other similar vectors, and Δt is a constant time step.

To construct the chemical diffusion model on an irregular grid such as a triangular grid, we subdivide the triangular grid into a finite number of non-overlapping control volumes, over which energy conservation is enforced in a discrete sense. Therefore, the construction of the chemical diffusion model on a triangular grid can be achieved by discretizing the chemical diffusion model on each control volume. Figure 9.1 shows a control volume (surrounded by the dot lines) constructed around point $\mathbf{P}_i$. The control volume consists of the centroids of the triangles adjacent to point $\mathbf{P}_i$ and the midpoints of the edges adjacent to point $\mathbf{P}_i$.

Considering Eq. (9.6) over the control volume shown in Fig. 9.1, and applying Gauss formula yield

$$\int_{S_i}\left(\frac{\partial C}{\partial t}+H\right)\mathrm{d}S=\int_{B_i}(\omega\nabla C)\cdot\mathbf{n}\mathrm{d}B \tag{9.10}$$

where S_i is the measure of the control volume at point $\mathbf{P}_i$, B_i is the closed boundary of S_i, "•" represents the dot product of two vectors and $\mathbf{n}$ is the outward unit normal vector at the boundary B_i.

The left side of Eq. (9.10) can be approximated as

$$\int_{S_i}\left(\frac{\partial C}{\partial t}+H\right)\mathrm{d}S=\left(\frac{\partial C_i}{\partial t}+H_i\right)S_i \tag{9.11}$$

Substituting Eq. (9.11) into Eq. (9.10) yields

$$\left(\frac{\partial C_i}{\partial t}+H_i\right)S_i=\int_{B_i}(\omega\nabla C_i)\cdot\mathbf{n}\mathrm{d}B \tag{9.12}$$

where C_i is the ion concentration at point $\mathbf{P}_i$.

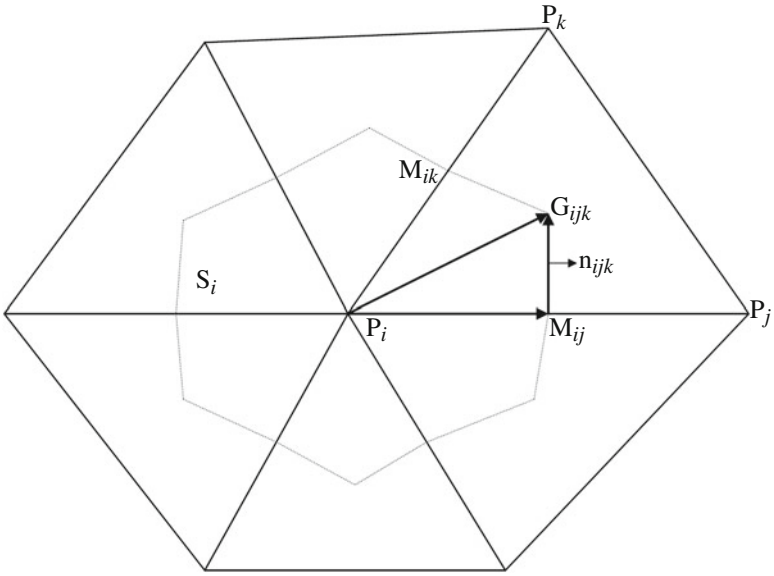

Fig. 9.1 A control volume over an irregular grid: the control volume consists of the centroids of the triangles adjacent to point $\mathbf{P}_i$ and the midpoints of the edges adjacent to point $\mathbf{P}_i$

By discretizing $\frac{\partial C_i}{\partial t}$, Eq. (9.12) may be rewritten as

$$C_i\left(t+\Delta t\right)=C_i(t)+\frac{\Delta t}{S_i}\int_{B_i}\left(\omega\nabla C_i(t)\right)\cdot\mathbf{n}\mathrm{d}B-H_i\Delta t \tag{9.13}$$

By discretizing B_i, Eq. (9.13) becomes

$$C_i\left(t+\Delta t\right)=C_i(t)+\frac{\Delta t}{S_i}\sum_{i\in N\left(\mathbf{P}_i\right)}\sum_{k\in N\left(\mathbf{P}_j\right)\cap N\left(\mathbf{P}_i\right)}\int_{M_{ij}G_{ijk}}\left(\omega\nabla C_i(t)\right)\cdot\mathbf{n}_{ijk}\mathrm{d}B-H_i\Delta t \tag{9.14}$$

where $N(\mathbf{P}_i)$ is the set of the neighbouring points of point $\mathbf{P}_i$ and $N(\mathbf{P}_j)$ is the set of the neighbouring points of point $\mathbf{P}_j$.

The gradient $\nabla C_i(t)$ over the small control volume defined by the triangle $\Delta\mathbf{P}_i\mathbf{P}_j\mathbf{P}_k$ may be written as

$$\begin{aligned}\nabla C_i(t)=&\frac{C_j(t)-C_i(t)}{\left\|\overrightarrow{\mathbf{P}_i\mathbf{P}_j}\times\overrightarrow{\mathbf{P}_i\mathbf{P}_k}\right\|^2}\left(\left\|\overrightarrow{\mathbf{P}_i\mathbf{P}_k}\right\|^2\overrightarrow{\mathbf{P}_i\mathbf{P}_j}-\left(\overrightarrow{\mathbf{P}_i\mathbf{P}_j}\cdot\overrightarrow{\mathbf{P}_i\mathbf{P}_k}\right)\overrightarrow{\mathbf{P}_i\mathbf{P}_k}\right)\\&+\frac{C_k(t)-C_i(t)}{\left\|\overrightarrow{\mathbf{P}_i\mathbf{P}_j}\times\overrightarrow{\mathbf{P}_i\mathbf{P}_k}\right\|^2}\left(\left\|\overrightarrow{\mathbf{P}_i\mathbf{P}_j}\right\|^2\overrightarrow{\mathbf{P}_i\mathbf{P}_k}-\left(\overrightarrow{\mathbf{P}_i\mathbf{P}_j}\cdot\overrightarrow{\mathbf{P}_i\mathbf{P}_k}\right)\overrightarrow{\mathbf{P}_i\mathbf{P}_j}\right)\end{aligned} \tag{9.15}$$

where "×" denotes the cross product of two vectors.

Substituting (9.15) into (9.14), there is

$$C_i\left(t+\Delta t\right)=C_i(t)+\frac{\omega\Delta t}{6S_i}\sum_{j\in N_i}\sum_{k\in N_i\cap N_j}\lambda_{ijk}\left(C_j(t)-C_i(t)\right)+\mu_{ijk}\left(C_k(t)-C_i(t)\right)-H_i\Delta t \tag{9.16}$$

where

$$\begin{aligned}\lambda_{ijk}&=\frac{\left\|\overrightarrow{\mathbf{P}_i\mathbf{P}_k}+\overrightarrow{\mathbf{P}_j\mathbf{P}_k}\right\|}{\left\|\overrightarrow{\mathbf{P}_i\mathbf{P}_j}\times\overrightarrow{\mathbf{P}_i\mathbf{P}_k}\right\|^2}\left(\left\|\overrightarrow{\mathbf{P}_i\mathbf{P}_k}\right\|^2\overrightarrow{\mathbf{P}_i\mathbf{P}_j}-\left(\overrightarrow{\mathbf{P}_i\mathbf{P}_j}\cdot\overrightarrow{\mathbf{P}_i\mathbf{P}_k}\right)\overrightarrow{\mathbf{P}_i\mathbf{P}_k}\right)\cdot\mathbf{n}_{ijk}\\ \mu_{ijk}&=\frac{\left\|\overrightarrow{\mathbf{P}_i\mathbf{P}_k}+\overrightarrow{\mathbf{P}_j\mathbf{P}_k}\right\|}{\left\|\overrightarrow{\mathbf{P}_i\mathbf{P}_j}\times\overrightarrow{\mathbf{P}_i\mathbf{P}_k}\right\|^2}\left(\left\|\overrightarrow{\mathbf{P}_i\mathbf{P}_j}\right\|^2\overrightarrow{\mathbf{P}_i\mathbf{P}_k}-\left(\overrightarrow{\mathbf{P}_i\mathbf{P}_j}\cdot\overrightarrow{\mathbf{P}_i\mathbf{P}_k}\right)\overrightarrow{\mathbf{P}_i\mathbf{P}_j}\right)\cdot\mathbf{n}_{ijk}\end{aligned} \tag{9.17}$$

Finally, the unit normal vector at the boundary $\overrightarrow{\mathbf{M}_{ij}\mathbf{G}_{ijk}}$ of the small control volume may be written as

$$\mathbf{n}_{ijk}=\frac{\left(\overrightarrow{\mathbf{P}_i\mathbf{P}_k}+\overrightarrow{\mathbf{P}_j\mathbf{P}_k}\right)\times\left[\overrightarrow{\mathbf{P}_i\mathbf{P}_j}\times\left(\overrightarrow{\mathbf{P}_i\mathbf{P}_j}+\overrightarrow{\mathbf{P}_i\mathbf{P}_k}\right)\right]}{\left\|\left(\overrightarrow{\mathbf{P}_i\mathbf{P}_k}+\overrightarrow{\mathbf{P}_j\mathbf{P}_k}\right)\times\left[\overrightarrow{\mathbf{P}_i\mathbf{P}_j}\times\left(\overrightarrow{\mathbf{P}_i\mathbf{P}_j}+\overrightarrow{\mathbf{P}_i\mathbf{P}_k}\right)\right]\right\|} \tag{9.18}$$

9.5 Internal Forces and Deformation Dynamics

Since the gradient of the concentration is the driving force for ion movement, the internal force can be described as

$$\mathbf{F}=-\omega\nabla_{\mathbf{P}}C \tag{9.19}$$

where "∇_P" represents the gradient with respect to the change in position.

For a regular grid, the internal force at a point can be directly obtained by discretizing the gradient operator at the point using a finite difference scheme. Therefore, the internal force at point P_i on a regular grid is:

$$\mathbf{F}_i=\omega\sum_{j\in N(\mathbf{P}_i)}\frac{\left|C_{\mathbf{P}_j}-C_{\mathbf{P}_i}\right|}{\left\|\overrightarrow{\mathbf{P}_i\mathbf{P}_j}\right\|}\mathbf{U}_{ij} \tag{9.20}$$

where $\mathbf{U}_{ij}=\frac{\overrightarrow{\mathbf{P}_i\mathbf{P}_j}}{\left\|\overrightarrow{\mathbf{P}_i\mathbf{P}_j}\right\|}$ and $\left|C_{\mathbf{P}_j}-C_{\mathbf{P}_i}\right|$ is the magnitude of the concentration change between point $\mathbf{P}_i$ and point $\mathbf{P}_j$.

For an irregular grid such as a triangular grid, since the discretization of the gradient operator is represented as Eq. (9.15), the internal force at point $\mathbf{P}_i$ is

$$\mathbf{F}_i = \omega \sum_{j \in N(\mathbf{P}_i)} \sum_{k \in N(\mathbf{P}_i) \cap N(\mathbf{P}_j)} \frac{C_j(t) - C_i(t)}{\left\| \overrightarrow{\mathbf{P}_i\mathbf{P}_j} \times \overrightarrow{\mathbf{P}_i\mathbf{P}_k} \right\|^2} \left(\left(\overrightarrow{\mathbf{P}_i\mathbf{P}_j} \cdot \overrightarrow{\mathbf{P}_i\mathbf{P}_k} \right) \overrightarrow{\mathbf{P}_i\mathbf{P}_k} - \left\| \overrightarrow{\mathbf{P}_i\mathbf{P}_k} \right\|^2 \overrightarrow{\mathbf{P}_i\mathbf{P}_j} \right)$$
$$+ \omega \sum_{j \in N(\mathbf{P}_i)} \sum_{k \in N(\mathbf{P}_i) \cap N(\mathbf{P}_j)} \frac{C_k(t) - C_i(t)}{\left\| \overrightarrow{\mathbf{P}_i\mathbf{P}_j} \times \overrightarrow{\mathbf{P}_i\mathbf{P}_k} \right\|^2} \left(\left(\overrightarrow{\mathbf{P}_i\mathbf{P}_j} \cdot \overrightarrow{\mathbf{P}_i\mathbf{P}_k} \right) \overrightarrow{\mathbf{P}_i\mathbf{P}_j} - \left\| \overrightarrow{\mathbf{P}_i\mathbf{P}_j} \right\|^2 \overrightarrow{\mathbf{P}_i\mathbf{P}_k} \right) \tag{9.21}$$

During the simulation, after computing the internal forces for each node, the Lagrange's equation of motion is used to update the node positions, and thus the following relationship may be written

$$m_i \frac{d^2\mathbf{P}_i}{dt^2} + \gamma_i \frac{d\mathbf{P}_i}{dt} + \mathbf{F}_i = \mathbf{G}_i \tag{9.22}$$

where $\mathbf{P}_i$ is the position vector of node i at time t, m_i and γ_i are the mass and damping constants of node i, respectively, $\mathbf{F}_i$ is the net internal force applied to node i at time t and $\mathbf{G}_i$ is the external force applied to node i at time t.

Equation (9.22) is solved by using an explicit integration scheme which does not require matrix inversion for updating each vertex position, and also has a simple implementation.

9.6 Implementation Results and Discussions

Experiments have been conducted to investigate the effect of isotropic, anisotropic and inhomogeneous deformation as well as nonlinear load-deformation of soft tissues. Interactive deformation of anatomical models of human body using a haptic device for surgery simulation is studied, and the comparison with the existing deformation methods is also discussed in this section.

9.6.1 Isotropic, Anisotropic, Inhomogeneous, Local and Large-Range Deformations

Experiments have been conducted to investigate isotropic, anisotropic and inhomogeneous deformation. Figure 9.2 illustrates the deformation of the isotropic material with 900 grid points ($\omega = 0.08$, mass = 10.0 and damping = 10.0). As shown in Fig. 9.2a, b, the material has a cubic shape with round corners in its rest state. Figure 9.2c, d are two different views of the material deformed under a compressive force of 3 kg.

Anisotropic deformation can be achieved by setting different diffusion coefficients in different directions. Figure 9.3 illustrates the deformation of an anisotropic

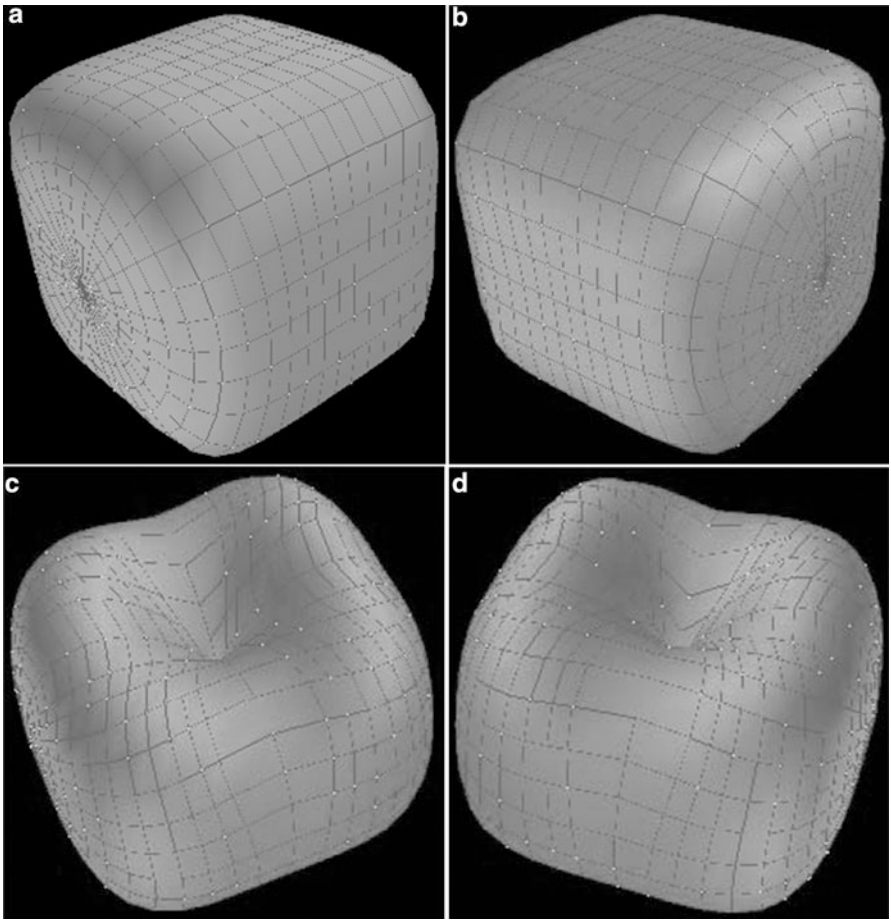

Fig. 9.2 Deformation of an isotropic material with a cubic and round-corner shape in its rest state: the material has a common diffusion coefficient ($\omega = 0.08$) at each point

material under the same external force as Fig. 9.2. The material has the same parameters as the material in Fig. 9.2 except that diffusion coefficients are different in the different parametric directions (ω in the latitudinal direction $= 0.08$ and ω in the longitudinal direction $= 0.24$). Compared to the isotropic deformation shown in Fig. 9.2, Fig. 9.3 shows that the material is deformed more in the longitudinal direction. This demonstrates the proposed methodology can simulate anisotropic deformation by simply setting different diffusion coefficients in different directions.

Inhomogeneous deformation can also be simulated by setting different diffusion coefficients at different points. Figure 9.4 illustrates the deformation of an inhomogeneous material under the same external force as Fig. 9.2. The material has the same parameters as the material in Fig. 9.2 except that the white portions ($\omega = 0.08$)

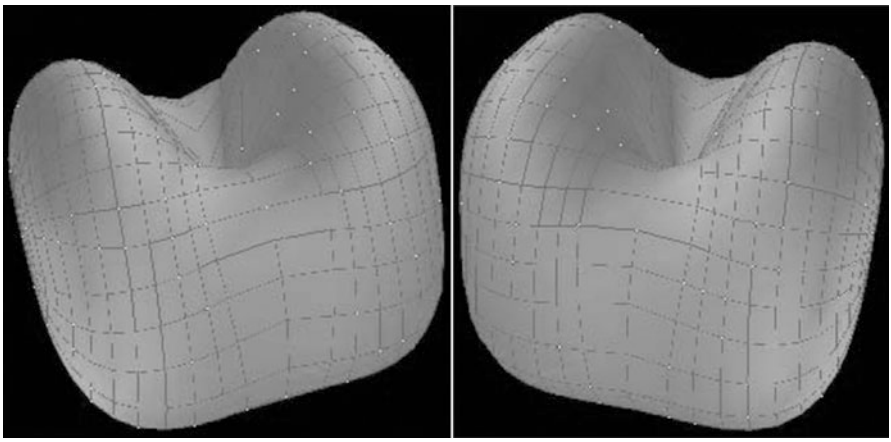

Fig. 9.3 Deformation of an anisotropic material by setting different diffusion coefficients in different directions (ω in the latitudinal direction $= 0.08$ and ω in the longitudinal direction $= 0.24$)

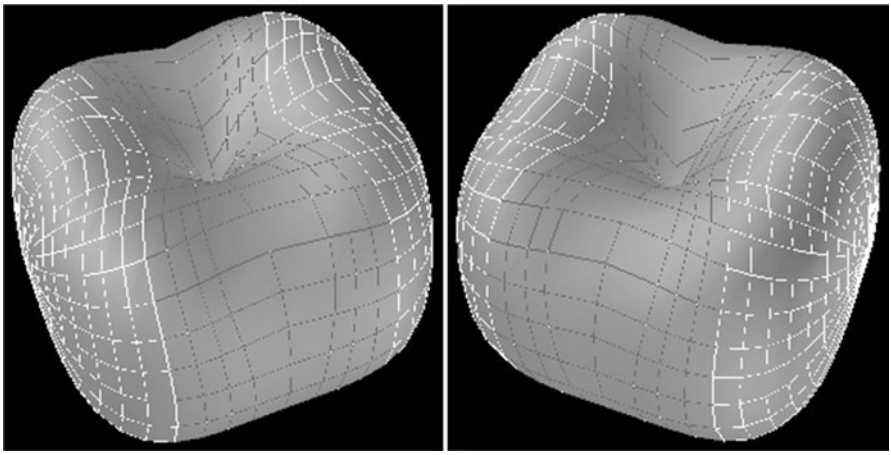

Fig. 9.4 Deformation of an inhomogeneous material by setting different diffusion coefficients at different points (ω in the *white portions* $= 0.08$ and ω in the *grey portion* $= 0.24$)

have a different diffusion coefficient from the grey portion ($\omega = 0.24$). As shown in Fig. 9.4, some of the white portions are deformed correspondingly during the deformation, and they also highlight the difference from the isotropic deformation shown in Fig. 9.2. Compared to the anisotropic deformation shown in Fig. 9.3, Fig. 9.4 illustrates that the material is deformed differently at the different points with different diffusion coefficients.

Local deformation can also be achieved with the proposed methodology by setting a very low diffusion coefficient to the points where small deformation is

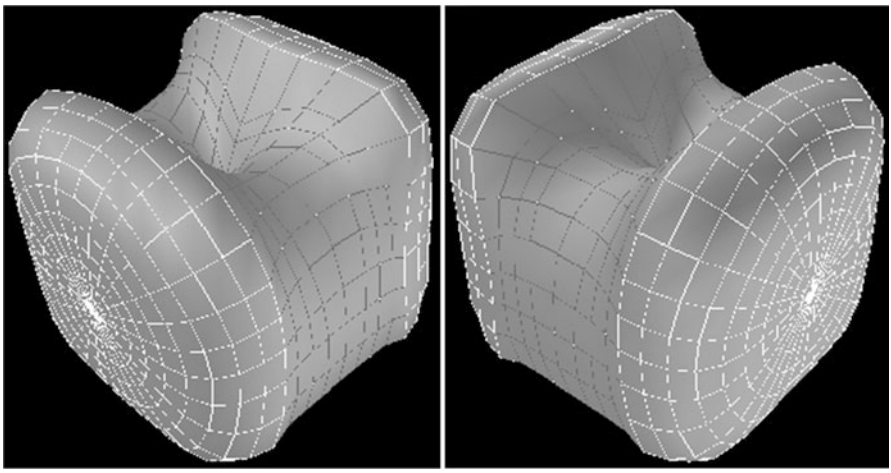

Fig. 9.5 Local deformation by using a very low diffusion coefficient: the *white portions* with a very low diffusion coefficient are not deformed

expected. Figure 9.5 illustrates an example of local deformation under the same external force as Fig. 9.2, in which the white portions with a very low diffusion coefficient are not deformed.

The proposed methodology has been further verified with real soft tissues. Figure 9.6 illustrates the simulated deformation behaviours of the proposed methodology against the experimental deformation behaviours of a lamb kidney. It can be seen that the simulation curve is in agreement with the experimental curve, and both deformations vary nonlinearly with the applied forces. This demonstrates that the proposed methodology can exhibit the mechanical behaviours of soft tissues. The nonlinear load–deformation relationship also reveals that the proposed methodology can accommodate large-range deformation.

9.6.2 Human Organ Deformation with Haptic Feedback

Laparoscopic surgery is much more difficult for surgeons than classical surgery. Surgeons lose the third dimension and use two long special surgical tools instead of their hands. Therefore, they must use all the clues provided to them to understand and reconstruct the scene in their minds. Force feedback is one of such clues, and its introduction in the surgery simulation greatly improves the overall realism of the simulation.

Real-time soft tissue simulation with force feedback for use in surgery simulation has been achieved by integration of a haptic device (PHANToM from Sensable Technologies) into the proposed methodology. The graphical rendering is achieved by the OpenGL graphics library, and the haptic rendering is achieved by the

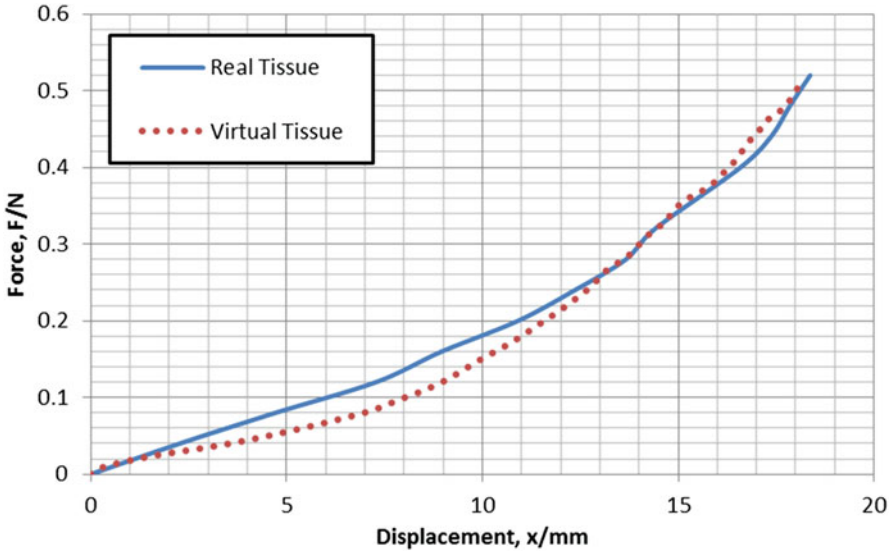

Fig. 9.6 Comparison between virtual and real soft tissue behaviours

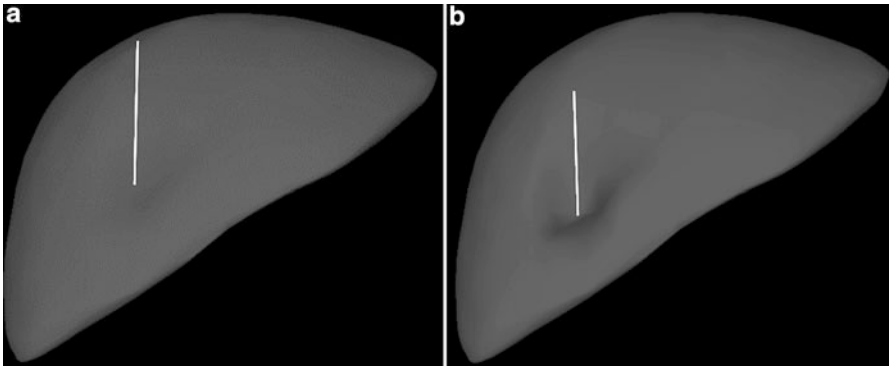

Fig. 9.7 Deformations of a virtual human liver model with haptic feedback by using a virtual probe

OpenHaptic toolkit from Sensable Technologies. Real-time interactive deformation of virtual human organs with force feedback has been performed by the proposed methodology. Figure 9.7 shows the deformation process of a virtual human liver model with force feedback by using a virtual probe and the final deformation result.

Table 9.1 Computational performance

Numbers of points	261	405	650	900	1100
Computational time (ms)	4.3	8.5	12.4	24.3	39.8
Frame rate (fps)	232.5	117.6	80.6	41.2	25.1

9.6.3 Computational Performance and Discussions

The proposed methodology has been implemented on an Intel Pentium (R) 2.8 GHz and 1.0G memory PC. With one external stimulus, the graphical update rate utilizing different numbers of mesh points is provided in Table 9.1. From Table 9.1, it can be seen that the graphical update rate is decreased with the increment of the mesh points. The visually satisfactory refresh rate of 30 Hz to maintain a realistic visual feedback (Sadd 2005) is achieved by meshes with less than about 1000 grid points. Since the correct visualization of an object such as the human liver requires at least 600 grid points (Zhang et al. 2014), this is sufficient to provide realistic visual feedback with the proposed methodology.

The haptic device requires forces to be updated at the rate of at least 1000 Hz for realistic force feedback (OpenHaptics ToolKit-Programmer's and Sensable 2004). It is observed that the force update rate is above 1000 Hz when the number of mesh points is relatively small. When the computational speed cannot cope with the haptic refresh rate any more, force extrapolation (Picinbono et al. 2002) is employed to improve the realism of force feedback by generating the missing forces from the previous time step.

The main difference of the proposed methodology from most of the existing deformation methods is that soft tissue simulation is carried out from the physic-ochemical viewpoint of soft tissues. It converts soft tissue deformation into a chemical–mechanical interaction problem, and thus the complex and expensive elastic computations are avoided. Compared with the common deformation methods such as mass-spring, FEM and BEM, the proposed methodology can deal with large-range deformation, while the common deformation methods can only handle small deformation. Compared with the few methods based on nonlinear strains for large-range deformations, such as explicit nonlinear FEM, large-range deformation is achieved by the nonlinear load–deformation relationship rather than the use of nonlinear strain in the explicit nonlinear FEM. The proposed methodology can handle both local and large-range deformation. In contrast, local deformation is difficult to achieve due to the use of nonlinear strain in the explicit nonlinear FEM. Furthermore, the proposed methodology can easily accommodate anisotropic and inhomogeneous deformation by simple modification of diffusion coefficients.

9.7 Conclusions

This paper presents a new methodology to conduct simulation of nonlinear soft tissue deformation from the physicochemical viewpoint of soft tissues. This methodology converts soft tissue deformation into chemical–mechanical interaction, and thus the complex and expensive elastic computations are avoided. It features chemical diffusion of mechanical load and non-rigid mechanics of motion to govern the simulation dynamics of soft tissue deformation. The proposed methodology can not only accommodate isotropic, anisotropic and inhomogeneous materials through simple modification of diffusion coefficients, but it can also accommodate local and large-range deformation.

Future research work will focus on the global validation of simulated deformation against real in vivo data of soft tissues. In fact, the validation should be based on in vivo measurement data on the mechanical properties of living tissues, due to the different behaviours between living tissues and non-living tissues. The measurement of in vivo mechanical data of soft tissues would be of great value for a full validation but is much more challenging to achieve experimentally. A minimally invasive in vivo measurement method for acquisition of mechanical data of soft tissues will be established for a full validation of deformation models.

References

Barbic, J., & James, D. L. (2005). Deformable models: Real-time subspace integration for St. Venant-Kirchhoff deformable models. *ACM Transactions on Graphics, 24*(3), 982–990.

Cakir, O., & Yazici, R. (2009). Real-time cutting simulation based on stiffness-warped FEM. In: *24th International Symposium on Computer and Information Sciences* (pp. 721–724), North Cyprus.

Choi, M. G., & Ko, H. S. (2005). Modal warping: Real-time simulation of large rotational deformation and manipulation. *IEEE Transactions on Visualization and Computer Graphics, 11*(1), 91–101.

Chou, P. C., & Pagano, N. J. (1967) *Elasticity*. Princeton, NJ: D. Van Nostrand Company.

Costa, I. F. (2012). A novel deformation method for fast simulation of biological tissue formed by fibers and fluid. *Medical Image Analysis, 16*, 1038–1046.

Duarte, V., Gonzalez, Y., & Cerrolaza, M. (2011). Boundary element simulation of bone tissue. *International Journal of Biomedical Engineering and Technology, 5*(2–3), 211–228.

Etzmuss, O., Gross, J., & Strasser, W. (2003). Deriving a particle system from continuum mechanics for the animation of deformable objects. *IEEE Transactions on Visualization and Computer Graphics, 9*(4), 538–550.

Fung, Y. C. (1993) *Biomechanics: Mechanical properties of living tissues* (2nd ed.). New York: Springer.

Lai, W. M., Hou, J. S., & Mow, V. C. (1991). A triphasic theory for the swelling and deformation behaviors of articular cartilage. *Journal of Biomedical Engineering, 113*(3), 245–258.

Mafi, R., & Sirouspour, S. (2014). GPU-based acceleration of computations in nonlinear finite element deformation analysis. *International Journal for Numerical Methods in Biomedical Engineering, 30*(3), 365–381.

Myers, E. R., Lai, W. M., & Mow, V. C. (1984). A continuum theory and an experiment for the ion-induced swelling behavior of articular cartilage. *ASME Journal of Biomechanical Engineering, 106*(2), 151–158.

Omar, M. N., Zhong, Y., Jazar, R. N., Subic, A., Smith, J., & Shirinzadeh, B. (2015). Soft tissue modelling with conical springs. *Bio-Medical Materials and Engineering, 26,* S207–S214.

OpenHaptics ToolKit-Programmer's Guide, Sensable Technologies (2004).

Patete, P., Iacono, M. I., Spadea, M. F., Trecate, G., Vergnaghi, D., Mainardi, L. T., et al. (2013). A multi-tissue mass-spring model for computer assisted breast surgery. *Medical Engineering and Physics, 35*(1), 47–53.

Peterlik, I., Sedef, M., Basdogan, C., et al. (2010). Real-time visio-haptic interaction with static soft tissue models having geometric and material nonlinearity. *Computers and Graphics – UK*, *34*(1), 43–54.

Picinbono, G., Lombardo, J.-C., Delingette, H., & Ayache, N. (2002). Improving realism of a surgery simulator: Linear anisotropic elasticity, complex interactions and force extrapolation. *Journal of Visualization and Computer Animation, 13*(3), 147–167.

Picinbono, G., Delingette, H., & Ayache, N. (2003). Non-linear anisotropic elasticity for real-time surgery simulation. *Graphical Models, 65*(5), 305–321.

Sadd, M. H. (2005). *Elasticity: Theory, applications, and numerics*. Amsterdam: Elsevier Butterworth Heinemann.

San-Vicente, G., Aguinaga, I., & Celigueta, J. T. (2012). Cubical mass-spring model design based on a tensile deformation test and nonlinear material model. *IEEE Transactions on Visualization and Computer Graphics, 18*(2), 228–241.

Schwartz, J.-M., Denninger, M., Rancourt, D., Moisan, C., & Laurendeau, D. (2005). Modelling liver tissue properties using a non-linear visco-elastic model for surgery simulation. *Medical Image Analysis, 9*(2), 103–112.

Taylor, Z. A., Crozier, S., & Ourselin, S. (2011). A reduced order explicit dynamic finite element algorithm for surgical simulation. *IEEE Transactions on Medical Imaging, 30*(9), 1713–1721.

Wu, J. Z., & Herzog, W. (2002). Simulating the swelling and deformation behaviour in soft tissues using a convective thermal analogy. *Biomedical Engineering Online, 1*(8), 8.

Zhang, J., Wang, J., Wang, X., & Feng, D. (2014). The adaptive FEM elastic model for medical image registration. *Physics in Medicine and Biology, 59*(1), 97–118.

Zhong, Y., Shirinzadeh, B., Alici, G., & Smith, J. (2006a). An autowave based methodology for deformable object simulation. *Computer-Aided Design, 38*(7), 740–754.

Zhong, Y., Shirinzadeh, B., Alici, G., & Smith, J. (2006b). A neural network methodology for deformable object simulation. *IEEE Transactions on Information Technology in Biomedicine, 10*(4), 749–762.

Zhong, Y., Shirinzadeh, B., Smith, J., & Gu, C. (2010). Thermal-mechanical based soft tissue deformation for surgery simulation. *International Journal of Advanced Robotics, 24*, 1719–1739.

Zhong, Y., Shirinzadeh, B., Smith, J., & Gu, C. (2012). Soft tissue deformation with reaction-diffusion process for surgery simulation. *Journal of Visual Languages and Computing, 23*(1), 1–12.

Zhu, B., & Gu, L. (2012). A hybrid deformable model for real-time surgical simulation. *Computerized Medical Imaging and Graphics, 36*(5), 356–365.